Coherent-hybrid STED: high contrast sub-diffraction imaging using a bi-vortex depletion beam

ANTÓNIO PEREIRA,[1,2,*] MAFALDA SOUSA,[1,2] ANA C. ALMEIDA,[1,2] LUÍSA T. FERREIRA,[1,2] ANA RITA COSTA,[1,2] MARCO NOVAIS-CRUZ,[1,2] CRISTINA FERRÁS,[1,2] MÓNICA MENDES SOUSA,[1,2] PAULA SAMPAIO,[1,2] MICHAEL BELSLEY,[3] AND HELDER MAIATO[1,2,4]

[1]i3S - Instituto de Investigação e Inovação em Saúde, Universidade do Porto, Rua Alfredo Allen, 208, 4200-135 Porto, Portugal
[2]IBMC - Instituto de Biologia Molecular e Celular, Rua Alfredo Allen, 208, 4200-135 Porto, Portugal
[3]Center of Physics, University of Minho, Campus de Gualtar, 4710-057 Braga, Portugal
[4]Cell Division Group, Experimental Biology Unit, Department of Biomedicine, Faculdade de Medicina, Universidade do Porto, Alameda Prof. Hernâni Monteiro, 4200-319 Porto, Portugal
*apereira@ibmc.up.pt

Abstract: Stimulated emission depletion (STED) fluorescence microscopy squeezes an excited spot well below the wavelength scale using a doughnut-shaped depletion beam. To generate a doughnut, a scale-free vortex phase modulation (2D-STED) is often used because it provides maximal transverse confinement and radial-aberration immunity (RAI) to the central dip. However, RAI also means blindness to a defocus term, making the axial origin of fluorescence photons uncertain within the wavelength scale provided by the confocal detection pinhole. Here, to reduce the uncertainty, we perturb the 2D-STED phase mask so as to change the sign of the axial concavity near focus, creating a dilated dip. By providing laser depletion power, the dip can be compressed back in three dimensions to retrieve lateral resolution, now at a significantly higher contrast. We test this coherent-hybrid STED (CH-STED) mode in x-y imaging of complex biological structures, such as the dividing cell. The proposed strategy creates an orthogonal direction in the STED parametric space that uniquely allows independent tuning of resolution and contrast using a single depletion beam in a conventional (circular polarization-based) STED setup.

1. Introduction

The capacity to label proteins and other macromolecules with highly specific fluorescent reporters makes fluorescence microscopy an essential tool in the life sciences. Although spatial resolution is conventionally limited to a half-wavelength in the far-field, techniques have been developed that evade this limit by exploiting the fact that the fluorescence microscope is not governed exclusively by optics laws, but involves a (generally nonlinear) sample response [1–6].

In one seminal example, STED microscopy exploits the nano-second excited-state time window by delivering a second, red-shifted, depletion beam (the 'STED' beam) to silence significant portions of the excited (diffraction-limited) fluorophore spot [1,7]. Although the depletion beam can equally lead to re-excitation, this is minimized if fluorophores that spontaneously undergo a rapid post-depletion decay are used [8,9] (or by employing coherent population inversion techniques [10]). In the standard implementation, the depletion beam is a dark spot surrounded by steep intensity gradients [11] - a 'doughnut'- that scans the sample along with the excitation beam. At each position, and if saturated depletion is reached, only a sub-diffraction-sized fluorophore ensemble survives the doughnut beam and fluoresces.

Although the fluorescence signal is diffracted as it travels to the detector, its origin - the target coordinate - can be looked up at a scanner-defined (sub-diffraction) resolution. With a resolution limited by technical details only, the use of favorable samples has allowed STED to reach better than 10nm lateral resolution using excitation/depletion wavelengths above 500nm [12].

A problem in single-objective, single-beam, STED (or more generally, RESOLFT implementations [13]) is that the two doughnut beams used in the field, z-STED and 2D-STED, have geometries that are rigid, while displaying contrasting performances regarding lateral resolution, axial resolution, signal-to-background ratio (SBR) and aberrations resilience. The z-STED mode for example, where a π-shifted top-hat phase mask modulates the depletion beam, generates a very strong axial confinement [7,14] but a comparatively low lateral confinement (see Fig. 1(a)). z-STED is also affected by the spurious signal emitted by undepleted excitation lobes ('ghosts') and by simple aberrations, such as an imprecision in mask scale definition which, by unbalancing the π-shifted contributions, fills the central 'zero' and attenuates the signal of interest [11,15]. This sensitivity to scale and to the other radial aberrations (such as spherical) often demands mask readaptation to imaging conditions, some of which may vary in the course of a bio-imaging 'session' (e.g. the refractive index mismatch between samples and the objective immersion medium, the depth of the structure under observation and the objective lens [15]). Ultimately, z-STED is typically used for cross-section (*x-z*) imaging only, where its notable axial resolution may prove decisive.

For the highest lateral resolution, a helical phase ramp ('vortex') phase mask [16] is used. This so-called 2D-STED mode (Fig. 1(b)) is regarded as a standard in STED microscopy, particularly when performing *x-y* imaging. 2D-STED maximizes lateral confinement for a given energy [11], suffers from low ghost noise and generates an aberration-resilient intensity-zero [16,17]. Crucially, the absence of a radial scale in the phase mask provides RAI, eliminating the scale mismatch-elicited noise that compromised z-STED. However, the feature that confers RAI to 2D-STED also determines that the vortex-generated dip is not a point, but a nodal line along the optical axis. Thus, in 2D-STED, it is still the detection pinhole that solely defines the axial response. The effective point-spread function (PSF) is thus a very thin but long (>λ) needle along the optical axis.

This rigid and complementary nature of the two STED modes prompted the use of beam superposition architectures. These two-beam (or many-beam) approaches allow a major improvement in depletion isotropy [18–20], which can be further improved by using radially or azimuthally-polarized depletion beams [21,22]. However, in addition to compound aberration effects [23,24] and alignment requirements at the nanometer scale, an incoherent superposition can never rectify a residual filling of the intensity-zero which may be present in either beam (usually the z-STED component). To provide an alternative to incoherent superpositions, the present work focuses on the definition of a single depletion beam to improve the 2D-STED axial response, aiming at increasing contrast in x-y STED imaging.

In this context, it is instructive to visualize a 'signal rescue' scenario as it is encountered in actual 2D-STED experiments. If the depletion laser power is gradually increased, the needle-shaped fluorescence source is eventually made so thin that a vanishingly small number of molecules remain in the 'on' state. This condition of 'excess resolution' is eventually reached even if an ideal beam with a perfect nodal line is used, or otherwise sooner. The recourse is to reduce back the laser power, which widens the parabolic dip, so that neighboring molecules are allowed to fluoresce. By doing this, the needle-shaped source dilates in all planes, recovering focal signal but also the unwanted background. Thus, the usual power-modulation protocol does not permit an independent tuning of lateral resolution and contrast. In principle, addition of a doughnut-geometry degree of freedom to the 'power-only' modulation could decouple control over these metrics.

Here, applying a RAI-assisted modulation to the vortex mask, we generate a depletion doughnut that dilates the dip primarily at the focal plane, providing focus-specific signal

selection, thus fundamentally changing the axial response. Dip dilation does not reflect a fundamental loss in lateral resolution. Instead, the transformed axial response sets the stage for a non-linear process (e.g., STED) to compress the PSF in a more isotropic manner. With both beam geometry and depletion non-linearity at hand, one can expect to achieve independent control over lateral resolution and depth sectioning.

2. Coherent-hybrid depletion beam

To test the concept, we aimed at defining a phase-only mask that generates a hollow depletion beam featuring a dilation at the focal plane. A comprehensive resource for hollow beam engineering [25–29] is the field of optical trapping, where these beams find application in manipulating low-refractive index particles. However, in optical trapping the absolute intensity-zero is less important than sophistication of the dielectric maps (e.g. for dynamic, multiple, tunable trap generation). In contrast, the major concern in STED bio-imaging is signal preservation, which demands one sharp dark spot. Thus, to create a dilated dip, we restrict ourselves to phase mask typologies providing a robust intensity-zero.
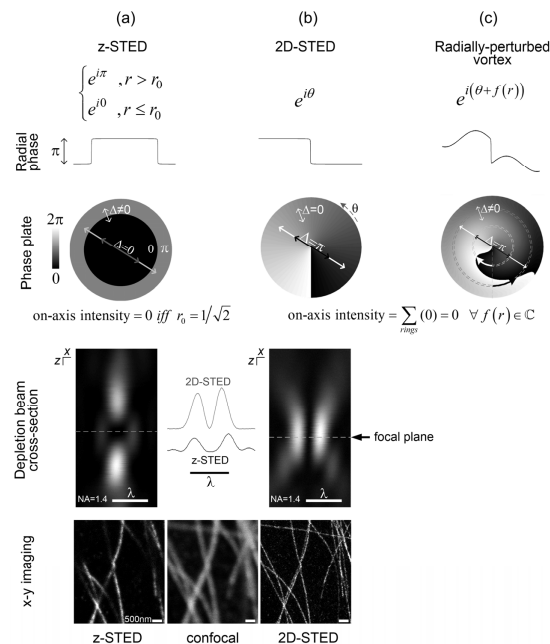

Fig. 1. Phase masks for the standard STED modes and for a 'radial vortex'. a) z-STED mask for mostly-axial confinement. b) 2D-STED mask for transverse confinement. c) An intensity-zero is warranted whenever a vortex-phase is added to an arbitrary radial-only function, *f(r)* (Appendix A). Off-axis radial phase gradients (∆=0) can be exploited to generate an axial gradient for STED confinement. The bottom rows show experimental cross-sections and focal profiles of z-STED and 2D-STED using gold-bead scattering (775nm wavelength, 1.4 NA objective) with corresponding x-y imaging of microtubule filaments.

A sufficient condition for aberration resilience (RAI) is a mask constructed as a radial tile of concentric annular regions, each one filled with a vortex phase of integer, equal-sign but possibly different, topological charge. That is so because each annular vortex produces an intensity-zero [30] even in the vectorial regime (e.g. using equal-handedness circular polarization; see Appendix A). Trivially, the full complement of annular vortices still yields an intensity-zero, irrespective of the annulus mutual phase (rotation) and amplitude (Fig. 1(c), Appendix A).

This annular tile is equivalent to the addition of a vortex to a radial-only function, obeying a 'radial vortex' condition, $\phi(r,\theta) = f(r) + \theta$, where $f(r)$ is an arbitrary function,

generally complex, of the distance to the optical axis r, and θ is the azimuthal angle. While the vortex component θ, provides RAI, $f(r)$ can represent, for example, a lens phase function (paraxial or non-paraxial defocus term), an imprecision in setting the mask scale, spherical aberration, a radial amplitude profile of the depletion beam or their arbitrary combination.

For our purposes, $f(r)$ provides the degree of freedom permitting a shift in the sign of the isophotes' concavity near the focal point (Fig. 2(a)), even if, by symmetry, the concavity vanishes at the optical axis. To achieve concavity inversion we choose a step function, justified by the fact that only an off-axis phase gradient (absent in the pure vortex mask, $\Delta = 0$ in Fig. 1(b)) can generate axially varying interference conditions, as in z-STED. However, in contrast to z-STED, where the step needs to be precisely located at a radius r_0 for scale matching ($r_0 = R/\sqrt{2}$ for a uniformly illuminated pupil of radius R), the vortex presence eliminates the constraint.
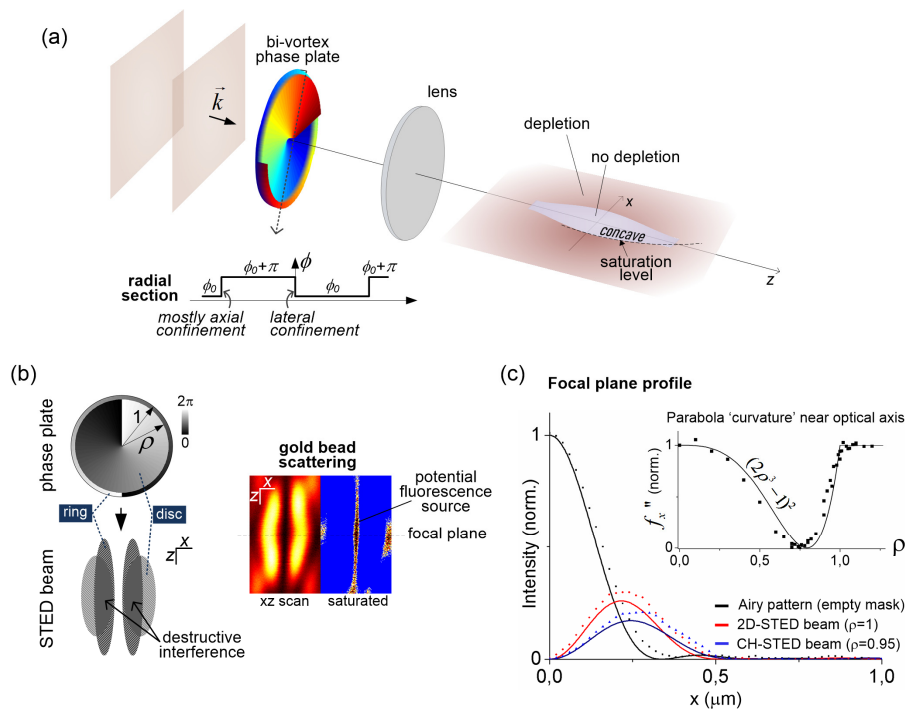

Fig. 2. (a) Simplified layout of the modified STED setup. (b) Interpretation and observation by gold bead scattering of the tunable dip generation. The scattering images are for an xz-scanned gold bead displayed with a linear and a saturated look-up table (LUT), the latter providing a heuristic preview of the effective fluorescence source at high saturation. (c) Data-points and paraxial theory (solid lines) for the depletion beam focal plane profile. In the inset, beam's geometrical confinement metric (second-order derivative of intensity) with experimental data and theory as a function of the bi-vortex radius, ρ. The single adjusted parameter (both in the main graph and in the inset) is a global vertical normalization factor.

A general expression for the phase disturbance imparted by the phase mask can be written as $M(r,\theta) = \exp(in\theta + ai\pi H(r-\rho))$ with H the Heaviside step function. This includes, as limiting cases, the z-STED ($n = 0$, $a = 1$, $\rho \cong 0.71R$) and the 2D-STED single vortex ($n = 1, \rho > R$) modes. In the particular case we focus on in this work ($n = 1, \rho < R$), the resultant is a 'bi-vortex' parameterized by ρ, the radius at which the vortex switches sign

(Fig. 2(b)). It can be noted that at a particular scale and amplitude modulation, the beam created by a bi-vortex phase would degenerate to the standard Laguerre-Gauss (LG$_{11}$) beam [31,32].

To gain insight on the diffraction pattern created by the bi-vortex, it can be seen that the contracted (inner) vortex alone would generate a correspondingly wider doughnut at the Fourier plane. The exposed peripheral vortex, which has the same handedness but is out-of-phase, would by its own generate an elongated and narrow dip [33], reminiscent of an inverted annular-shaped aperture PSF [34,35]. The resultant is a long narrow dip, dilated specifically at the focal plane region. This tunable dark spot can be seen as arising from the destructive interference of the beam crests generated by the individual vortices (Fig. 2(b)).

We call the beam created by the bi-vortex mask a 'coherent-hybrid (CH-) STED' beam, as it amounts to the addition of a 2D-STED mask to a rescaled z-STED mask. Clearly, instrumental imprecisions in setting the desired ρ (or even the phase step magnitude) do not compromise the radial vortex condition for an intensity-zero (Appendix A), anticipating operational ruggedness regarding central fluorescence preservation.

Although vectorial diffraction is required for a complete analysis [36], assumption of sufficient polarization symmetry conditions (as imparted by circular polarization), allows the paraxial approximation to deliver a quantitative insight into the effect of the bi-vortex on lateral resolution. The intensity profile at the focal plane (Fig. 2(c)) in the neighborhood of the optical axis is, in the parabolic approximation, given by (Appendix B)

$$\lim_{x \to 0} I_{bi-vortex} \to I_0 \left(\frac{2\pi NA}{3\lambda} x \right)^2 \left(2\rho^3 - 1 \right)^2, \tag{1}$$

where I_0 represents the on-axis focal plane intensity created by the circular pupil without a phase mask, NA is the (beam width-dependent) effective numerical aperture of the focusing system, λ is the STED beam wavelength in vacuum and x is the distance to the optical axis. At this expansion level (parabolic approximation), the only difference relative to the single vortex (2D-STED) mask is the factor $\left(2\rho^3 - 1 \right)^2$. In contrast, the z-STED profile structure starts at fourth order, providing low (and fixed) geometrical confinement. Experimental data for the parabola concavity near the optical axis fits well this paraxial approximation (inset in Fig. 2(c)), with the slight left-shift being likely caused by the finite width of the STED beam incident on the objective.

3. Experimental results

To create a true intensity-zero using a high-NA objective, 2D-STED setups typically use a circularly polarized depletion beam matching the vortex handedness (or charge). This configuration (as well as other rotationally symmetric polarization states) warrants cancellation of the axial component of the electric field at the optical axis. The same applies for each annular vortex of a CH-STED mask, making existing STED setups adequate for CH-STED microscopy. Here, we used a confocal gated-STED (Abberior Instruments 'Expert Line') featuring 40 MHz-modulated excitation (560 and 640nm) and depletion (775nm) beams, coupled to a Nikon Ti microscope. The bi-vortex phase pattern was imprinted on a phase-only spatial light modulator (LCOS, Hamamatsu) on top of a factory-set flat-field correction phase map, with an additional grating being used to diffract the beam off zero-order. A 4f-system is used to image the SLM plane at the back focal plane of an oil-immersion 1.4NA 60x plan-apochromatic objective (Nikon, Lambda Series). All acquisitions were made with a confocal pinhole size of 0.8 Airy units and an APD detector gate (800ps-8ns).

z-scans of 40nm-diameter fluorescently-labeled nano-beads (Crimson beads (Abberior), excitation 640nm), show that the CH-STED PSF depletes the ghost spots efficiently as

compared to z-STED (Fig. 3(a)) and provides the desired dip around the geometrical focus (absent in 2D-STED). The effect of depletion energy redistribution is therefore a specific suppression of out-of-focus fluorescence signal – an ampoule-shaped PSF (Fig. 3(b), bottom), which should be more suitable than 2D-STED for imaging thick and complex environments.
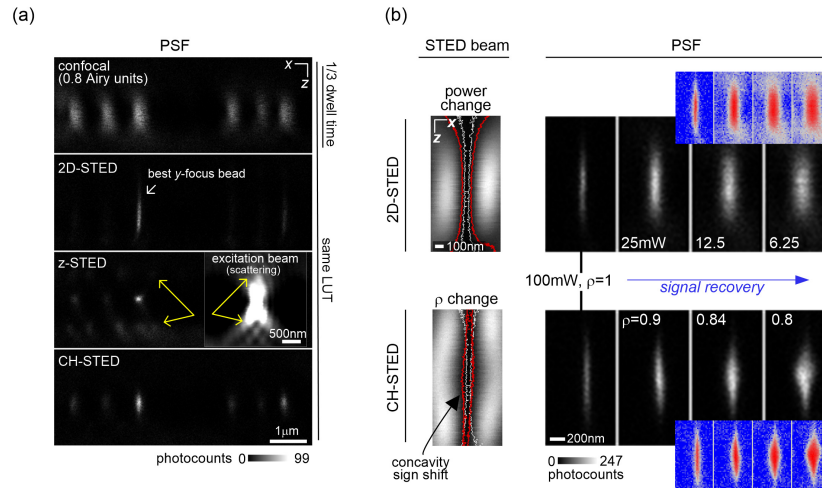

Fig. 3. STED modes PSFs. (a) Nano-bead fluorescence xz-scans in different STED modes (same LUT display). The inset highlights the origin of the excited ghosts that are poorly depleted by the z-STED beam. (b) Left: gold bead scattering cross-section in 2D-STED and CH-STED with isophote lines defining saturation contours. White-to-red represent signal rescue in 2D-STED (depletion power change) and in CH-STED (ρ change). Red and white isophotes in the CH-STED panel are for the same intensity value and are therefore representative of an actual 2D- to CH-STED transition. Right: effective PSF in the two STED regimes. Red-blue images (same LUT) are log-intensity versions that highlight background noise.

We tested interphase cell and mitotic spindle imaging (see sample preparations in Appendix D) with CH-STED using the geometrical transformation only: the constant-power mode (Fig. 4). Here, a focus-specific signal rescue (coupled to a loss in lateral resolution) is expected. Fluorescence signal from interpolar microtubules and kinetochore fibers (microtubule bundles attached to chromosomes), which are immersed in a noisy environment, emerges after switching to CH-STED. In brighter spindles (Fig. 4(a)), the gain is attributed to relative background decrease, whilst at lower photon counts (Fig. 4(b)), the signal increase after transition becomes relevant also against detection noise. Microtubules in less dense meshworks clearly show the expected loss in lateral resolution, but even here the SBR is markedly increased (Fig. 4(c), see z-stack acquisition in Visualization 1).

To assess performance we used elementary PSF metrics (defined in Fig. 5(a) inset) in the optical sectioning range, $\rho \approx 0.8-1$, as well as at a varying STED power. Width was measured at the focal plane (D_0) and at a plane defocused by one Rayleigh range ($z_R = 260$nm), the standard measure of the Gaussian beam's (half-) depth of focus. It is observed that, while the PSF undergoes the usual scale transformation at varying STED power (Fig. 5(a)) [37,38], a shape transformation towards $D_z < D_0$ is observed when ρ is varied (Fig. 5(b)).
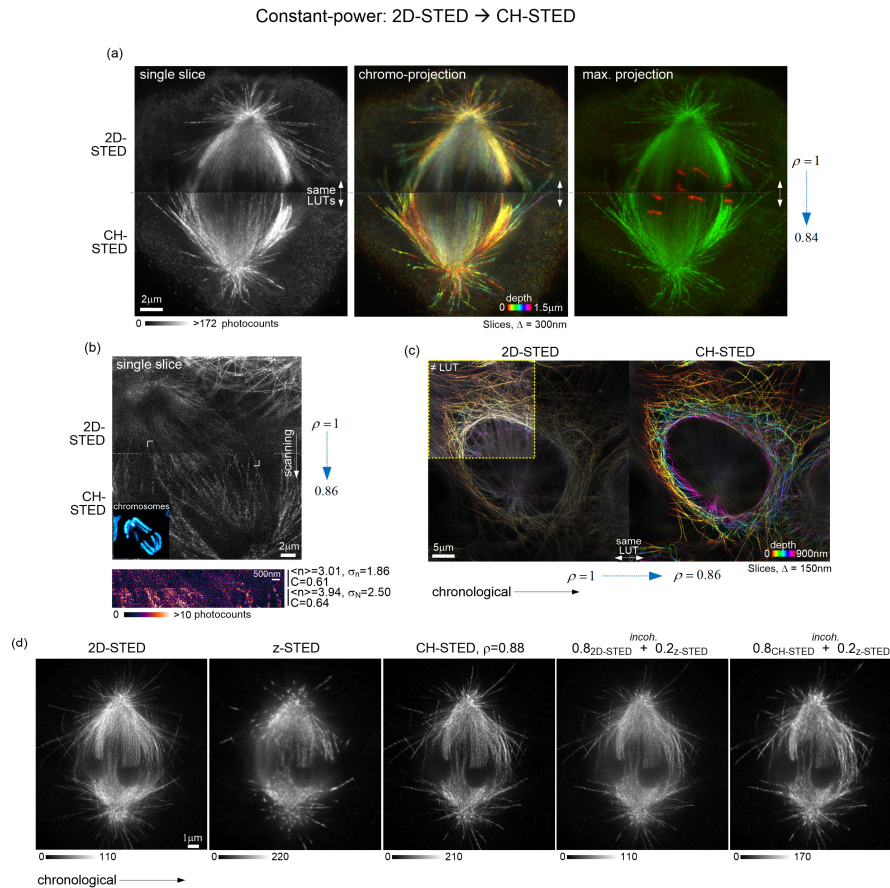
Fig. 4. 2D-STED to CH-STED transition in constant-power mode with all acquisition parameters (apart from the phase mask) kept constant. (a) Single-slice and projections from a z-stack acquisition of a tubulin-labeled Indian muntjac dividing cell in metaphase, with a kinetochore marker shown in the right panel (red). Top- and bottom-halves are independent, vertically adjacent, acquisitions. (b) Low-signal Indian muntjac dividing cell in anaphase (chromosome staining in the inset) and zoomed ROI at the 2D to CH transition zone. Photon standard deviation, average and their ratio for the top and bottom halves are displayed. (c) Chromo-projection from a z-stack (Visualization 1) of a tubulin-labeled U2OS interphase cell. Color definition is a readout for optical sectioning. (d) Indian muntjac mitotic spindle in all single-beam and incoherent superposition modes. In (c) and (d), where a single object is consecutively imaged, a left-right acquisition sequence is followed.

Lateral resolution CH-STED data is in agreement with theoretical calculations (Fig. 5(b)), where a parabolic approximation to the depletion beam proves insufficient (see Appendix B). The high-order expansion required to generate the theoretical curve reflects the fact that, in CH-STED, power and resolution are not anymore univocally related (even for a given fluorophore type), making the fluorescent profile sensitive to the detailed structure of the depletion beam whenever high STED power is used for high sectioning (i.e., lateral resolution lower-end, $\rho < 0.9$).
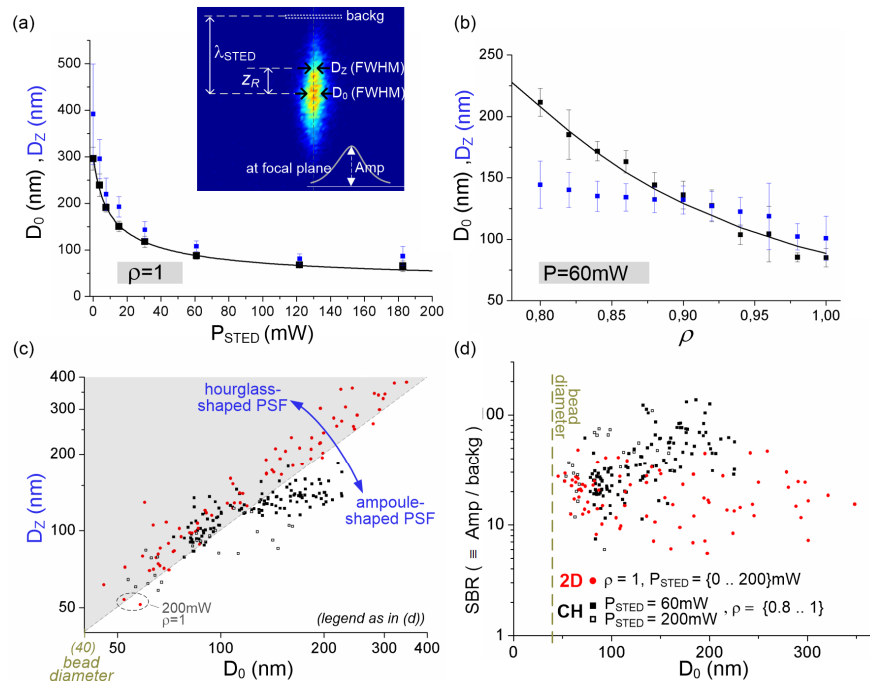
Fig. 5. CH-STED vs. 2D-STED axial confinement and background suppression using 40-nm fluorescent beads. (a) PSF lateral dimension using the full-width half-maximum (FWHM) criteria (mean ± s.d., n = 10 beads per datapoint) at and away from the focal plane in 2D-STED as a function of STED laser average power (at back focal plane). In the inset, metrics for assessing performance, where the defocused plane chosen for measuring confinement is at a Rayleigh range distance (z_R = 260nm) from the focal plane. (b) PSF lateral dimension (mean ± s.d., n = 10 beads per datapoint) at and away from the focal plane in CH-STED as a function of ρ, using an intermediate-range STED power (60mW). (c) Scatter plot comparison of 2D-STED and CH-STED (at 60mW and 200mW) using a common parameter (D_0) as the independent variable. Each datapoint represents one bead. Axes were cropped at 400nm, leaving three 2D-STED (red) datapoints not displayed (used and accounted for in quantifications in (a)). (d) Relative background suppression estimate using the focal plane Gaussian curve fit amplitude relative to an average background value at a one wavelength distance from the focal plane (as displayed in (a) inset).

For a parametric comparison of 2D-STED and CH-STED, D_Z was measured as a function of a common independent variable - lateral resolution, D_0. In these scatter plots (Fig. 5(c)), where each point represent one nano-bead, the instrumental parameters P_{STED} and ρ are implicit variables that probe the $D_0 \times D_z$ space. The bottom-right half-space is populated by experimental PSFs that get narrower away from the focus ('ampoule-shaped'), as opposed to the hourglass-shaped PSF typical of confocal and 2D-STED microscopes. In addition to the progressive geometrical confinement, CH-STED more efficiently attenuates the integrated signal emitted from out-of-focus planes (Fig. 5(d)), as measured by the PSF amplitude relative to a background signal measured at a one-wavelength axial distance (defined in Fig. 5(a)).

Thus far, we used either P_{STED} or ρ modulation to tune the PSF (Figs. 3(b) and 4). Naturally, the two-dimensional parameter space can be explored. Using the simplified parabolic dip approximation and a first-order approximation to the depletion process [37], the combined effect of ρ and P_{STED} yields a generalized STED equation for lateral resolution,

$$R \cong \frac{\lambda}{2NA\sqrt{1+\left(1-2\rho^3\right)^2 \dfrac{P_{STED}}{P_{SAT}}}}, \qquad (2)$$

where P_{SAT}, a saturation power characteristic of the sample, sets the scale for resolution improvement. From Eq. (2), a constant-resolution mode arises naturally (Fig. 6(a)) through the combination of a decreasing ρ with an increased depletion power. Here, the extra power recovers lateral resolution with increased optical sectioning. As required, Eq. (2) tends to the usual STED equation [37,38] if ρ tends to 1 or 0.
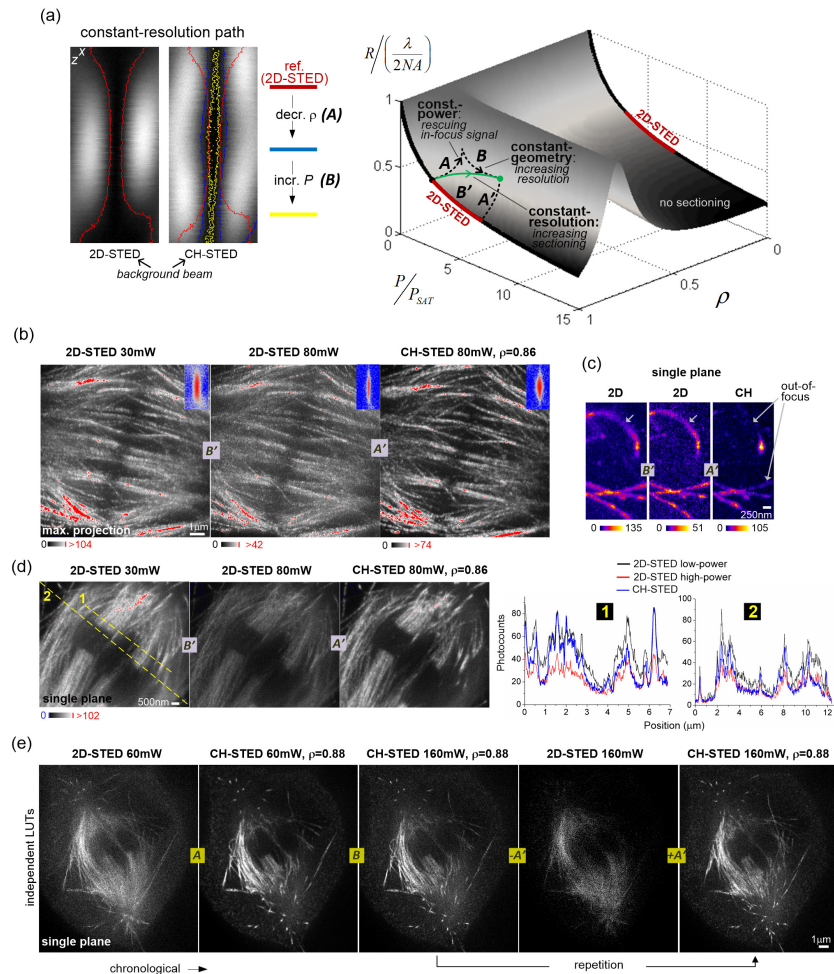
Fig. 6. (a) Left: STED beam cross-sections with contour lines showing signal rescue (path A) followed by resolution rescue (path B); Right: Surface displaying theoretical resolution under the parabolic approximation (Eq. (2)). Example trajectories for the three base modes are outlined: constant-power (A or A'), constant-geometry (B or the 2D-STED case B') and constant-resolution (green line). (b) Projection of an anaphase spindle in a tubulin filament-labeled U2OS cell. Blue-red insets are pictorial examples of the PSF cross-section in each condition (taken from Fig. 3(b)) (c) Single slice image of astral microtubules in a prometaphase U2OS cell showing suppression of defocused portions in CH-STED. (d) Central region of a tubulin-labeled Indian muntjac mitotic spindle. Photocount profiles (right) correspond to the yellow dashed lines. (e) Tubulin-labeled Indian muntjac mitotic spindle along alternative paths in the theoretical surface. Independent LUTs are used. All panels in this figure follow a left-right acquisition sequence, with all unstated settings kept constant.

A three-acquisition sequence was followed in order to standardize comparative imaging: constant-geometry (of which 2D-STED is one particular case), constant-power and constant-resolution (Fig. 6(a)). To avoid 'chronological' artifacts that might over-estimate CH-STED performance (e.g. by photo-bleaching), CH-STED was always acquired after 2D-STED (and z-STED) acquisitions. Different biological contexts (Figs. 6(b)-6(e) and Visualization 2) indicate that entering the CH-STED regime provides background rejection at high focal signal level. This is shown in photo-count profiles (line-plots in Fig. 6(d)) displaying a high CH-STED signal relative to the constant-power counterpart (the high-power 2D-STED) and a low background relative to the constant-resolution counterpart (the low-power 2D-STED), which

amounts to a an increased dynamic range. Other samples, such as neuronal structural proteins, nucleoporins and tubulin in other cell stages (Appendix C and Visualization 2) generally deliver increased structural information when observed with CH-STED. An exception is sub-wavelength-thickness objects, where a regime closer to 2D-STED ($\rho > 0.95$) should be used.

As a practical corollary, if SBR is judged to be too low in a given 2D-STED acquisition, entering CH-STED is proposed as the default path (Fig. 6(e)), provided deleterious photo-physical effects (e.g. photo-bleaching) do not call for a decrease in STED beam power.

4. Discussion and conclusion

We introduced CH-STED as a perturbation to 2D-STED that dilates and contracts the nodal line of the depletion beam as it crosses the focal plane. This simple geometrical modulation, parameterized by the bi-vortex radius ρ, allowed a focus-specific fluorescence signal selection. Lateral resolution was shown to scale inversely with the geometrical and optical factor, $\left(2\rho^3 - 1\right)^2 P_{STED}$. When required, the resolution decrease caused by setting ρ below 1 can be recovered by increasing P_{STED}, now accompanied by an improved depth sectioning.

Fundamentally, CH-STED deviates from the conventional search for best lateral resolution, shifting focus towards a tunable compromise between resolution and SBR, with 2D-STED remaining as the limiting case where $\rho = 1$. Unless sub-diffraction sectioning is provided by the sample itself [39] or by using evanescent excitation fields, such as in TIRF-STED [40], it is unlikely that the exact value $\rho = 1$ is the best choice in any given context within imaging-based, time-domain [41–44] or lithography [45] STED or RESOLFT variants. Very thin objects will generally benefit from approaching, instead of reaching, $\rho = 1$. These results indicate that, as a general practical rule for the microscope user, the STED beam power should be increased all the way up to a point in which photo-damaging effects are still considered negligible, even if SBR is already severely compromised. Having defined such set-point, SBR is recovered by decreasing ρ.

CH-STED background suppression is low compared to z-STED, but it displays higher lateral resolution and a more efficient depletion of the secondary excitation lobes (Fig. 3(a)), which is shown to be particularly relevant in x-y imaging (Fig. 4(d)). Alternative strategies for background reduction, such as double-depletion STED (termed STEDD) [46], which directly estimates background signal, can be used along with CH-STED for a cumulative improvement in contrast.

Increased power exacerbates photo-damage, a concern in STED microscopy which led to technical advances [47–51] and conceptual generalizations for the use of an optical doughnut [52,53]. Still, whenever a doughnut is used, the highest intensities at the doughnut crest, which are evidently the most photo-damaging for the sample, are too far away from the center to contribute significantly to resolution improvement [50]. The interesting point here is that the unwelcome intensity overshoot of the classical doughnut gets dispersed orthogonally (along the optical axis) when ρ is decreased below unity, thus decreasing the intensity variance of the STED beam. This decreased overshoot in CH-STED will likely translate into decreased photo-toxicity in a constant-power transition (Fig. 4).

Finally, we note that CH-STED does not require modifications in the polarization state (circular, with the proper handedness) of the STED beam used in typical STED setups. If an SLM is used for beam phase modulation, CH-STED implementation is immediate. Static phase plates are still a simple and very high-performance alternative also for CH-STED. In this case, zoom optics have to be used to persistently image the bi-vortex plate at the back focal plane of the objective at a variable magnification. Independent of implementation details, a CH-STED beam can be incoherently combined to a z-STED beam (Fig. 4(d)) to provide improved sectioning.

Appendix A: High-NA radial vortices

Following the seminal work of Richards and Wolf [36], we express the electric field components near the focus of an aplanatic lens system as:

$$
\begin{bmatrix} E_+(s,\varphi,z) \\ E_-(s,\varphi,z) \\ E_z(s,\varphi,z) \end{bmatrix} = \frac{-iA}{2\pi} \int_0^{\alpha} d\theta \int_0^{2\pi} d\phi \cos^{1/2}\theta \sin\theta M(\theta,\phi)
$$

$$
\times \begin{bmatrix} (\cos\theta-1)\exp(2i\phi) \\ \cos\theta+1 \\ -\sqrt{2}\sin\theta\exp(i\phi) \end{bmatrix} \tag{3}
$$

$$
\times \exp\{ik[z\cos\theta + s\sin\theta\cos(\phi-\varphi)]\}
$$

Here we have taken the incident wave to be a right-hand circularly polarized monochromatic plane wave while $M(\theta,\phi)$ is the phase mask used to generate the STED beam, assumed to be placed at the entrance pupil characterized by the spherical polar coordinates (θ,ϕ). The upper limit on the polar angle integration is related to the numerical aperture of the lens system by $n\sin(\alpha) = NA$, while the coordinates in image space are $\mathbf{r} = (s,\varphi,z)$ centered on the position of the paraxial focus.

The bi-vortex is a member of a family of phase masks that can be called 'radial vortices', characterized by a phase $g(\theta) + n\phi$. Here $g(\theta)$ is an arbitrary function that depends only on the polar angle θ, and n is a non-zero integer defining the vortex order or charge. Within this family one can envision a set of infinitely thin annular rings, each at a given polar angle, modulated by a nth order vortex. In this case the integrals over the azimuthal angle can be written as

$$
\int_0^{2\pi} d\phi \exp(ig(\theta)+in\phi) \begin{bmatrix} (\cos\theta-1)\exp(2i\phi) \\ \cos\theta+1 \\ -\sqrt{2}\sin\theta\exp(i\phi) \end{bmatrix}. \tag{4}
$$

$$
\times \exp\{ik[z\cos\theta + s\sin\theta\cos(\phi-\varphi)]\}
$$

Using the Bessel function identity [54]

$$
\exp(iq\sin x) = \sum_{m=-\infty}^{\infty} J_m(q)\exp(imx), \tag{5}
$$

one can readily show that the azimuthal integrals in Eq. (4) reduce to

$$
2\pi \exp[ig(\theta)+ikz\cos\theta]
$$

$$
\times \begin{bmatrix} (\cos\theta-1)e^{i(n+2)\varphi} J_{n+2}(ks\sin\theta) \\ (\cos\theta+1)e^{in\varphi} J_n(ks\sin\theta) \\ -\sqrt{2}\sin\theta e^{i(n+1)\varphi} J_{n+1}(ks\sin\theta) \end{bmatrix} \tag{6}
$$

For positive n, i.e. when the helicity of the vortex mask is equal to that of the incident circular polarization, all of the Bessel functions have a positive order and vanish on-axis where $s = 0$. Contrary to non-zero disturbances, which may vanish by coherent addition,

superimposed zero disturbances will always yield an intensity-null, meaning that the bi-vortex intensity profile will always vanish on-axis irrespective of the type of radial perturbation.

Examples of radial perturbations to the depletion beam are:

i) an imprecision in setting a = 1 for the bi-vortex aπ step function,

ii) an imprecision in setting the desired bi-vortex radius ρ,

iii) a spherical aberration term,

iv) a defocus term,

v) a complex $g(\theta)$ accounting for, for example, the finite width depletion beam.

In conclusion, although spherical aberration or any radial perturbation will alter the off-axis intensity profile, which can affect the STED depletion in areas not highly saturated, the on-axis intensity remains zero.

Appendix B: Focal plane bi-vortex STED beam profile

To arrive at a simple expression characterizing the focal plane bi-vortex STED beam profile we employ a simplified model, assuming coherent monochromatic plane waves incident on the phase mask placed at the entrance pupil of the lens system. Treating the lens system as a simple thin lens in the paraxial approximation, the $\cos^{1/2}\theta \simeq 1$ and the incident polarization will be maintained through the image space to a good approximation. Then the electric field amplitude of the STED beam in the focal plane can be estimated within the Fresnel approximation by [34],

$$U_f(\mathbf{u}) = \frac{\exp\left[i(k/2f)|\mathbf{u}|^2\right]}{i\lambda f} \\ \times A\int d^2\mathbf{x}\, M(\mathbf{x})\exp\left[-i\frac{k}{f}\mathbf{x}\bullet\mathbf{u}\right] \tag{7}$$

Here, $\mathbf{x}$ denotes the coordinates in the mask plane, while $\mathbf{u}$ are those in the focal plane, f is the effective focal length of the objective, A is the amplitude of the incident plane wave, λ is wavelength and $M(\mathbf{x})$ the bi-vortex mask function

$$M_{bV}(\mathbf{x}) = \begin{cases} -e^{i\theta} & 0 \le r \le \rho R \\ e^{i\theta} & \rho R < r \le R \end{cases}, \quad 0 \quad r > R \tag{8}$$

The radius of the circular entrance pupil is R while we have used (r,θ) to denote the polar coordinates in the mask plane and will take (s,ϕ) to be the corresponding polar variables in the focal plane. Within the Fresnel approximation, the electric field distribution in the focal plane is determined by the Fourier transform of the mask function. The Fourier transform of a single vortex function of radius R can be shown to be

$$\mathscr{M}_{sV}(R;s,\phi) = \int d^2\mathbf{x}\, M_{sV}(\mathbf{x})\exp\left[-i\frac{k}{f}\mathbf{x}\bullet\mathbf{u}\right], \\ = -ie^{i\varphi}\frac{\pi^2 fR}{ks} \\ \times\left[J_1\left(\frac{ksR}{f}\right)H_0\left(\frac{ksR}{f}\right) - J_0\left(\frac{ksR}{f}\right)H_1\left(\frac{ksR}{f}\right)\right] \tag{9}$$

where J_n and H_n are respectively the nth order Bessel and Struve functions [55]. Here M_{sV} is equal to M_{bV} of Eq. (8) in the limit that $\rho \to 0$ or equivalently $\rho \to 1$. Consequently, for the coherent superposition bi-vortex one has

$$\mathcal{M}_{bV}\left(\rho, R; s, \phi\right) = \mathcal{M}_{sV}\left(R; s, \phi\right) - 2\mathcal{M}_{sV}\left(\rho R; s, \phi\right). \tag{10}$$

Expanding the resulting expression in a Taylor series about $s = 0$, one can readily show that to leading order in s, the focal plane intensity of the bi-vortex near the optical axis varies as

$$\lim_{s \to 0} I_{bi-vortex}\left(\rho, R; s\right) \to I_0 \left(\frac{2\pi NA}{3} s\right)^2 \left(2\rho^3 - 1\right)^2. \tag{11}$$

Here we have used the paraxial approximation for the numerical aperture, $NA \approx \lambda k R / \left(2\pi f\right)$, while I_0 represents the on axis focal plane intensity created by a circular pupil of radius R (without a phase mask). At this expansion level (parabolic approximation) the only difference relative to the single vortex (2D-STED) mask is the factor of $\left(2\rho^3 - 1\right)^2$. However, it should be noted that the on-axis curvature of the bi-vortex focal plane intensity pattern becomes increasingly smaller as ρ approaches $\sqrt[3]{0.5} \approx 0.794$ as can readily be seen in Fig. 7.
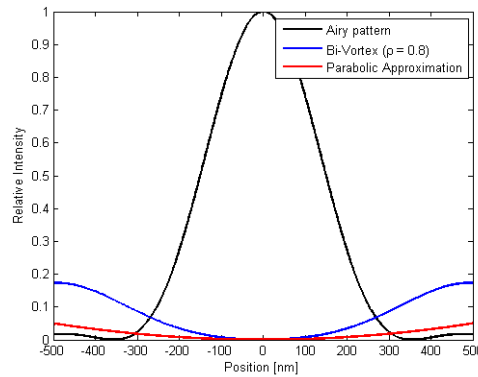

Fig. 7. Intensity variation of the bi-vortex focal plane profile near the point at which the on-axis curvature vanishes, together with the leading term in the Taylor expansion (parabolic approximation).

Because of this vanishing curvature, using the parabolic approximation to estimate the full width half maximum (FWHM) of the fluorescence profile can lead to significant errors. To arrive at the theoretical curve shown in Fig. 5(b), the following procedure was followed. First the nominal FWHM of the focal plane fluorescence was determined through a nonlinear least squares fit of the experimental profile to a Gaussian function, providing a FWHM of 294nm with a 95% confidence interval of [289 300]. This information was used to constrain the fit of the 2D-STED focal plane FWHMs as a function of the STED beam power shown in Fig. 5(a). We assumed that the convolution with the finite fluorescent bead diameter could be accounted for by adding a constant width in quadrature with the conventional 2D-STED FWHM power dependence:

$$\left(FWHM\right)^2 = \frac{\left(FWHM_0\right)^2}{1 + P/P_{Sat}} + B^2. \tag{12}$$

Using a weighted nonlinear least squares fitting routine with the nominal FWHM constrained to lie within the above 95% confidence interval of the focal plane fluorescence profile, we obtained the following parameters $FWHM_0 = 300\ nm$, $P_{sat} = 5\ mW$, $B = 32nm$ with an adjusted R-squared value of 0.995. To obtain the FWHM profile for the CH-STED we assumed a simple rate equation model for the excitation and de-excitation of the fluorescing molecular state. In the focal plane this leads to an emitted fluorescence profile of the form

$$I_{CH-STED}\left(\lambda_{ex},\lambda_{STED},\rho,R;s\right) = \frac{I_{ex}\left(\lambda_{ex},R;s\right)}{1+\alpha I_{bV}\left(\lambda_{STED},\rho,R;s\right)} \tag{13}$$

Here $I_{ex}\left(s\right)$ represents the excitation profile (Airy function), $I_{bV}\left(s\right)$ the bi-vortex intensity profile corresponding to

$$I_{bV}\left(\lambda_{STED},\rho,R;s\right) = \frac{I_0}{(2\pi R^2)^2}\left|\mathcal{M}_{bV}\left(\lambda_{STED},\rho,R;s\right)\right|^2. \tag{14}$$

The parameter α was set by requiring that the FWHM of the profile given by Eq. (13) with $\rho = 1$ corresponds to that measured using the 2D-STED configuration with an incident power of 60mW, yielding $\alpha = 59$. Numerically determining the resulting FWHM from Eq. (13) as ρ is varied and including the bead convolution contribution B added in quadrature, leads to the curve shown in Fig. 8, reproduced as the theoretical curve of Fig. 5(b). For comparison, the prediction of the conventional expression for FWHM reduction based on the on-axis curvature (the parabolic approximation of Eq. (11)) is also included.
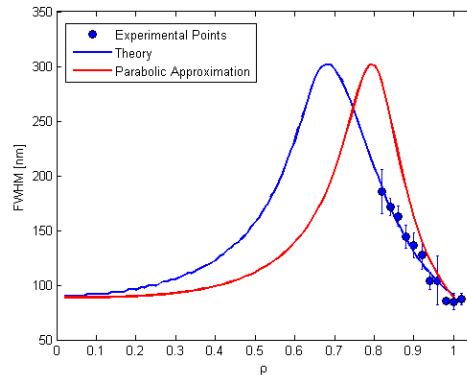

Fig. 8. Predicted variation of the focal plane fluorescence spot size as the CH-STED parameter ρ is varied. The parabolic approximation deviates significantly from the experimental values for values of ρ below 0.9.
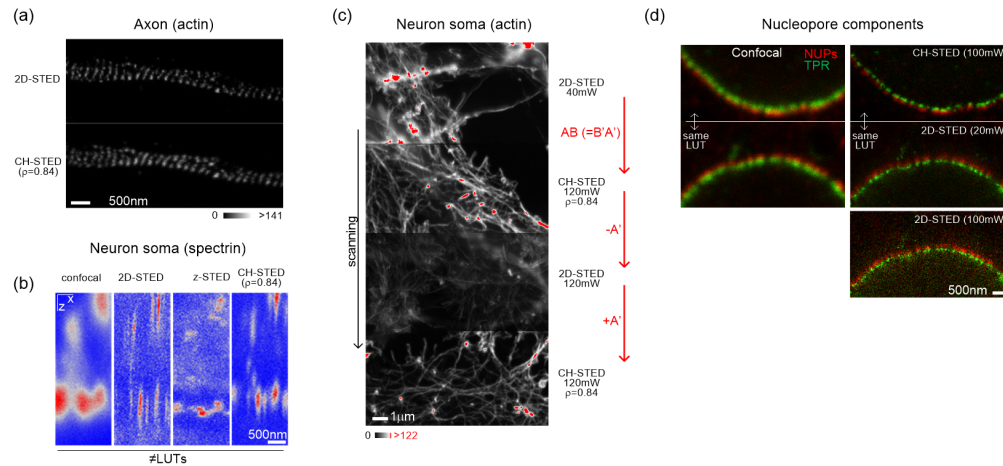
Appendix C: CH-STED examples in neurons and nucleopores

Fig. 9. (a) Actin-labeled axon. Transition to CH-STED displays mostly a loss in lateral resolution. In these thin structures (<λ) SBR improvement is less significant. (b) Standard and CH-STED modes compared to confocal in a cross-section acquisition of a spectrin-labeled neuron cell body. (c) Transition between STED modes during scanning (vertical slow axis) following the paths outlined in Fig. 6(a). The object is the peripheral area of an actin-labeled neuron cell body. (d) Confocal and dual-channel STED imaging of nuclear pore components in HeLa cells.

Appendix D: Materials and methods

Microscope setup. An Abberior Instruments 'Expert Line' gated-STED was used coupled to a Nikon Ti microscope. An oil-immersion 60x 1.4NA Plan-Apo objective (Nikon, Lambda Series) and pinhole size of 0.8 Airy units were used in all acquisitions. The system features 40 MHz modulated excitation (405, 488, 560 and 640nm) and depletion (775nm) lasers. The depletion beam (approx. 1ns-long) is modulated by a phase-only SLM (Hamamatsu) which allows arbitrary imprinting of phase masks, as well as the incoherent superposition of two arbitrary depletion beams. A 4f-system is used to image the phase mask at the back focal plane of the objective, where a slight overfilling of the beam balances doughnut energy with geometrical confinement (defining an effective, below nominal, NA). To a higher or lesser extent, the effective NA defined by the beam width smoothens the focused beam-shape response to ρ variation. Because absolute power levels were not required for this study, all STED laser powers were measured integrating the whole beam cross-section before hitting the objective. The microscope's detectors are avalanche photodiode detectors (APDs) which were used to gate the detection between 800ps and 8ns. To prevent saturation, acquisition settings (laser power levels, dwell time) were always chosen so that the maximum photo-detection count-rate was below 10MHz. Abberior's Imspector software, which is used to control the microscope settings and the acquisition process, allows the SLM to be controlled externally. A Python script was used to imprint the bi-vortex. The pattern is actually imprinted on top of a factory-set flat-field correction phase map and a grating structure is used to diffract the beam off the zero-order diffraction caused (SLM fill factor: 96%). The 2D grating periods were tuned every couple of hours to warrant co-alignment of the excitation and STED beams. In some images (Figs. 4(b) and 9(c)), the SLM pattern was switched during scanning (slow scan axis always vertical).

Beads analysis. xzy-scans of gold nano-beads were performed by detecting the 775nm scattered signal with a PMT positioned before the confocal pinhole with a 20nm pixel size in all dimensions. Depletion beam profile and concavity determination (Fig. 2(c)) were done in ImageJ by intensity profiling a 3μm-long 60nm-wide line. 2nd-order derivative (Fig. 2(c))

was determined in Matlab by doing a parabolic fit to the eleven data-points around the profile dip (200nm window). The portion of the SLM imaged on the effective back focal plane of the objective, which must be known for defining the pupil unit circle, is estimated at 108 SLM pixels by inspection of the data in the inset of Fig. 2(c). To characterize the microscope PSF in 2D-STED and CH-STED, 10 fluorescent nano-beads were xz-scanned for each condition (STED power or SLM bi-vortex radius variation), amounting to a total number of 200 beads. Acquisition pixel size was set to 20nm both dimensions. No acquisitions were excluded. For each bead image, a rough PSF center position was set to allow definition of a relevant ROI matrix (2.8x0.6μm) around the bead image, which was then exported to Matlab for quantification. A Gaussian fit to the x-projected matrix was used to determine a 'focal plane' position. The pixel line corresponding to the calculated focal plane was summed to the adjacent lines (defining a 60nm-wide axial averaging) for FWHM and Amplitude (Figs. 5(a)-5(c) and Fig. 5(d), respectively) determination by gaussian fitting. The goodness of fit was evaluated using the coefficient of determination R^2, with results higher than 0.90. The same procedure (Gaussian fit after 3-line averaging) was used to determine the out-of-focus (D_z) width, at a Rayleigh range distance of 260nm (13 image pixels) from the focal plane. Background estimation (required to generate Fig. 5(d)) was done by averaging the pixel line photo-counts (600nm-long) at a distance λ_{STED} from the focal plane. Results are presented as (mean)±(standard deviation) of 10 beads for each condition (Figs. 5(a) and 5(b)).

Imaging sequence and display. All images are 'raw' (subjected to linear histogram adjustments only, always starting at 0 photocounts) or, when stated, projections of z-stacks (Figs. 4(a), 4(c) and 6(b)). Whenever more than one acquisition is shown for the same object, CH-STED was always acquired last (Figs. 4(c), 6(b)-6(d), 9(a)-9(b) and 9(d)). In Figs. 4(d) and 6(e), the longer acquisition sequences are explicitly stated. Whenever a single gray-scale bar or color bar is shown, it applies to all images in the set. In those image pairs which share the LUT but for which an intensity scale is not shown, a '*same LUT*' label was used associating the images. Images acquired by shifting the STED mode during scanning are a single image (Figs. 4(b) and 9(c), which therefore share the LUT. Chromo-projection (Fig. 4(c)) was created using the 'Temporal Color Code' function in Fiji with the 'Spectrum' LUT. Intensity colorbars used in blue-grey-red images use the 'Phase' LUT. The independent top-half and bottom-half acquisitions (each one is an independent z-stack acquisition) in Fig. 4(a) were aligned manually, amounting to a vertical shift of 330nm (11 image pixels).

Indian muntjac cells (IM). IM fibroblasts, immortalized with human hTERT (pBabe puro hTERT, kind gift from Jerry W Shay), were grown in Minimum Essential Media (MEM) (Gibco, Life Technologies), supplemented with 10% FBS (Gibco, Life Technologies), 2mM L-Glutamine (Alfagene) at 37 °C in humidified conditions with 5% CO2. IM fibroblast cells were seeded on fibronectin-coated coverslips 2 days before the experiment. Cells were incubated with 20 μM MG-132 (Calbiochem) for 50 minutes before fixation, in order to enrich the mitotic population. After fixation with 4% Paraformaldehyde and 0.25% Glutaraldehyde (Electron Microscopy Sciences), the cells were quenched with a 0.1% solution of Sodium Borohydrate in PBS and extracted using PBS-0,5% TritonX (Sigma-Aldrich). The coverslips were incubated with the primary antibodies [anti-human centromere antiserum 1:150 (Fitzgerald); anti-tyrosinated tubulin 1:150 (MCA77G, AbD Serotec)] in blocking solution for 1h at room temperature. After washing with PBS-0.1%Tween, coverslips were incubated with the secondary antibodies (Abberior STAR 580 and STAR RED 1:100) for STED microscopy. DAPI was then added for 5 minutes in PBS- 0.1% Tween 1:50,000 (4'6'-Diamidino-2-phenylindole, Sigma Aldrich). Coverslips were washed in PBS and sealed on glass slides using mounting medium (20 nM Tris pH 8, 0.5 N-propyl gallate, 90% glycerol).

U2OS cells. Human U2OS were cultured in DMEM (Gibco) supplemented with 10% fetal bovine serum (FBS, Gibco), at 37° C onto 22x22 mm coverslips. Fixation was performed using a solution of 4% (v/v) paraformaldehyde (Electron microscopy sciences) and 0.25%

(v/v) glutaraldehyde (Electron microscopy sciences) for 10 minutes. Autofluorescence was quenched using freshly prepared 0.1% (w/v) sodium borohydride (Sigma) for 10 minutes followed by cell permeabilization with phosphate buffer saline (PBS) supplemented with 1% Triton-X100 (Sigma-Aldrich) for 10 minutes. Immunolabeling was performed using rat anti-tyrosinated tubulin (1:200, clone YL1/2, MCA77G, AbD Serotec) and human anti-centromere antibody (1:200, kindly provided by Bill Earnshaw) diluted in PBS supplemented with 20% FBS and fluorescently labelled antibodies anti-rat STAR RED (1:200, Abberior) and anti-human STAR 580 (1:200, Abberior) diluted in PBS supplemented with 20% of FBS. DNA was counterstained with 4',6-Diamidino-2-phenylindole (DAPI, 1:50 000, Sigma Aldrich). Coverslips were mounted in glass slides using home-made mounting medium (20 nM Tris pH 8, 0.5 N-propyl gallate, 90% glycerol).

Neurons. Hippocampal neuron cultures from Wistar rats were performed as described (Kaech and Banker, 2006). Briefly, hippocampi from embryonic day 18 pups were digested for 15 min in 0.06% porcine trypsin solution (Sigma, T4799), triturated, and plated at 12,500 cells/well in 24 well-plates containing glass coverslips pre-coated with poly-L-lysine (50 μg/mL; Sigma, P2636). Neurons were cultured in Neurobasal medium (Invitrogen) supplemented with B27 (Gibco), 1% penicillin/streptomycin (Gibco) and L-Glutamine (2 mM; Gibco). At DIV8, cells were washed with PBS, fixed in 4% Paraformaldehyde in PBS (pH 7.4) for 20 min at room temperature, permeabilized with 0.1% Triton X-100 for 5 min, quenched with 200 mM ammonium chloride for 5 min, and blocked in 5% FBS for 1 hour. Primary mouse anti-βII-spectrin (1:200 in blocking buffer; BD Biosciences, cat#612562) was incubated overnight at 4°C and secondary anti-mouse STAR635P (1:200 in blocking buffer; Abberior, cat#2-0002-007-5) was subsequently incubated for 1 hour at room temperature. Incubation with phalloidin STAR635 (300 nM in PBS; Abberior, cat#2-0205-002-5) was performed for 1 hour at room temperature. Coverslips were mounted in 80% glycerol.

HeLa cells. HeLa were grown in Dulbecco's Modified Eagle Medium (DMEM) (Gibco, Life Technologies), supplemented with 10% FBS (Gibco, Life Technologies), at 37 °C in humidified conditions with 5% CO2. HeLa cells were seeded on coverslips one day before the experiment. After the fixation with 4% Paraformaldehyde in PBS pH 7.4 the cells were extracted using PBS-0.3% TritonX (Sigma-Aldrich). After short washes in PBS with 0.1% TritonX and blocking with 10% FBS in PBS with 0.1% Triton X, all primary antibodies were incubated at 4°C overnight (NUPS Abcam 24609 – Mouse 1:100; TPR NB100-2867 – Rabbit 1:100). The cells were then washed with PBS containing 0.1% TritonX and incubated with the respective secondary antibodies for 1h at room temperature (Abberior anti-rabbit STAR580 1:100; anti-mouse STAR 635P 1:100) for STED microscopy. Coverslips were washed in PBS with 0.1% TritonX and sealed on glass slides using mounting medium (20nM Tris pH 8, 0.5 N-propyl gallate, 90% glycerol).

Funding

References

1. S. W. Hell and J. Wichmann, "Breaking the diffraction resolution limit by stimulated emission: stimulated-emission-depletion fluorescence microscopy," Opt. Lett. **19**(11), 780–782 (1994).
2. R. Heintzmann, T. M. Jovin, and C. Cremer, "Saturated patterned excitation microscopy--a concept for optical resolution improvement," J. Opt. Soc. Am. A **19**(8), 1599–1609 (2002).
3. M. G. Gustafsson, "Nonlinear structured-illumination microscopy: wide-field fluorescence imaging with theoretically unlimited resolution," Proc. Natl. Acad. Sci. U.S.A. **102**(37), 13081–13086 (2005).
4. S. T. Hess, T. P. Girirajan, and M. D. Mason, "Ultra-high resolution imaging by fluorescence photoactivation localization microscopy," Biophys. J. **91**(11), 4258–4272 (2006).

5.   E. Betzig, G. H. Patterson, R. Sougrat, O. W. Lindwasser, S. Olenych, J. S. Bonifacino, M. W. Davidson, J. Lippincott-Schwartz, and H. F. Hess, "Imaging intracellular fluorescent proteins at nanometer resolution," Science **313**(5793), 1642–1645 (2006).
6.   M. J. Rust, M. Bates, and X. Zhuang, "Sub-diffraction-limit imaging by stochastic optical reconstruction microscopy (STORM)," Nat. Methods **3**(10), 793–795 (2006).
7.   T. A. Klar, S. Jakobs, M. Dyba, A. Egner, and S. W. Hell, "Fluorescence microscopy with diffraction resolution barrier broken by stimulated emission," Proc. Natl. Acad. Sci. U.S.A. **97**(15), 8206–8210 (2000).
8.   M. Dyba and S. W. Hell, "Focal spots of size lambda/23 open up far-field fluorescence microscopy at 33 nm axial resolution," Phys. Rev. Lett. **88**(16), 163901 (2002).
9.   M. Leutenegger, C. Eggeling, and S. W. Hell, "Analytical description of STED microscopy performance," Opt. Express **18**(25), 26417–26429 (2010).
10. T. Kaldewey, A. V. Kuhlmann, S. R. Valentin, A. Ludwig, A. D. Wieck, and R. J. Warburton, "Far-field nanoscopy on a semiconductor quantum dot via a rapid-adiabatic-passage-based switch," Nat. Photonics **12**(2), 68–72 (2018).
11. J. Keller, A. Schönle, and S. W. Hell, "Efficient fluorescence inhibition patterns for RESOLFT microscopy," Opt. Express **15**(6), 3361–3371 (2007).
12. E. Rittweger, K. Y. Han, S. E. Irvine, C. Eggeling, and S. W. Hell, "STED microscopy reveals crystal colour centres with nanometric resolution," Nat. Photonics **3**(3), 144–147 (2009).
13. M. Hofmann, C. Eggeling, S. Jakobs, and S. W. Hell, "Breaking the diffraction barrier in fluorescence microscopy at low light intensities by using reversibly photoswitchable proteins," Proc. Natl. Acad. Sci. U.S.A. **102**(49), 17565–17569 (2005).
14. J. Arlt and M. J. Padgett, "Generation of a beam with a dark focus surrounded by regions of higher intensity: the optical bottle beam," Opt. Lett. **25**(4), 191–193 (2000).
15. J. Heine, C. A. Wurm, J. Keller-Findeisen, A. Schönle, B. Harke, M. Reuss, F. R. Winter, and G. Donnert, "Three dimensional live-cell STED microscopy at increased depth using a water immersion objective," Rev. Sci. Instrum. **89**(5), 053701 (2018).
16. P. Török and P. Munro, "The use of Gauss-Laguerre vector beams in STED microscopy," Opt. Express **12**(15), 3605–3617 (2004).
17. S. Deng, L. Liu, Y. Cheng, R. Li, and Z. Xu, "Effects of primary aberrations on the fluorescence depletion patterns of STED microscopy," Opt. Express **18**(2), 1657–1666 (2010).
18. B. Harke, C. K. Ullal, J. Keller, and S. W. Hell, "Three-dimensional nanoscopy of colloidal crystals," Nano Lett. **8**(5), 1309–1313 (2008).
19. B. R. Patton, D. Burke, D. Owald, T. J. Gould, J. Bewersdorf, and M. J. Booth, "Three-dimensional STED microscopy of aberrating tissue using dual adaptive optics," Opt. Express **24**(8), 8862–8876 (2016).
20. K. Y. Han and T. Ha, "Dual-color three-dimensional STED microscopy with a single high-repetition-rate laser," Opt. Lett. **40**(11), 2653–2656 (2015).
21. Y. Xue, C. Kuang, S. Li, Z. Gu, and X. Liu, "Sharper fluorescent super-resolution spot generated by azimuthally polarized beam in STED microscopy," Opt. Express **20**(16), 17653–17666 (2012).
22. Y. Xue, C. Kuang, X. Hao, Z. Gu, and X. Liu, "A method for generating a three-dimensional dark spot using a radially polarized beam," J. Opt. **13**(12), 125704 (2011).
23. J. Antonello, E. B. Kromann, D. Burke, J. Bewersdorf, and M. J. Booth, "Coma aberrations in combined two- and three-dimensional STED nanoscopy," Opt. Lett. **41**(15), 3631–3634 (2016).
24. J. Antonello, D. Burke, and M. J. Booth, "Aberrations in stimulated emission depletion (STED) microscopy," Opt. Commun. **404**, 203–209 (2017).
25. X. Weng, X. Gao, H. Guo, and S. Zhuang, "Creation of tunable multiple 3D dark spots with cylindrical vector beam," Appl. Opt. **53**(11), 2470–2476 (2014).
26. C. Alpmann, M. Esseling, P. Rose, and C. Denz, "Holographic optical bottle beams," Appl. Phys. Lett. **100**(11), 111101 (2012).
27. Y. Zhang, "Generation of three-dimensional dark spots with a perfect light shell with a radially polarized Laguerre-Gaussian beam," Appl. Opt. **49**(32), 6217–6223 (2010).
28. Z. Zhang, H. Fan, H.-F. Xu, J. Qu, and W. Huang, "Three-dimensional focus shaping of partially coherent circularly polarized vortex beams using a binary optic," J. Opt. **17**(6), 065611 (2015).
29. L. Gong, W. Liu, Q. Zhao, Y. Ren, X. Qiu, M. Zhong, and Y. Li, "Controllable light capsules employing modified Bessel-Gauss beams," Sci. Rep. **6**(1), 29001 (2016).
30. W. Condell, "Fraunhofer diffraction from a circular annular aperture with helical phase factor," J. Opt. Soc. Am. A **2**(2), 206–208 (1985).
31. Y. Kozawa and S. Sato, "Dark-spot formation by vector beams," Opt. Lett. **33**(20), 2326–2328 (2008).
32. A. M. Yao and M. J. Padgett, "Orbital angular momentum: origins, behavior and applications," Adv. Opt. Photonics **3**(2), 161–204 (2011).
33. B. Wang, J. Shi, T. Zhang, X. Xu, Y. Cao, and X. Li, "Improved lateral resolution with an annular vortex depletion beam in STED microscopy," Opt. Lett. **42**(23), 4885–4888 (2017).
34. M. Born and E. Wolf, *Principles of optics: electromagnetic theory of propagation, interference and diffraction of light* (Elsevier, 2013).
35. C. Sheppard and Z. Hegedus, "Axial behavior of pupil-plane filters," J. Opt. Soc. Am. A **5**(5), 643–647 (1988).

36. B. Richards and E. Wolf, "Electromagnetic Diffraction in Optical Systems. 2. Structure of the Image Field in an Aplanatic System," Proc R Soc Lon Ser-A **253**, 358–379 (1959).
37. B. Harke, J. Keller, C. K. Ullal, V. Westphal, A. Schönle, and S. W. Hell, "Resolution scaling in STED microscopy," Opt. Express **16**(6), 4154–4162 (2008).
38. V. Westphal and S. W. Hell, "Nanoscale resolution in the focal plane of an optical microscope," Phys. Rev. Lett. **94**(14), 143903 (2005).
39. A. Punge, S. O. Rizzoli, R. Jahn, J. D. Wildanger, L. Meyer, A. Schönle, L. Kastrup, and S. W. Hell, "3D reconstruction of high-resolution STED microscope images," Microsc. Res. Tech. **71**(9), 644–650 (2008).
40. T. J. Gould, J. R. Myers, and J. Bewersdorf, "Total internal reflection STED microscopy," Opt. Express **19**(14), 13351–13357 (2011).
41. L. Kastrup, H. Blom, C. Eggeling, and S. W. Hell, "Fluorescence fluctuation spectroscopy in subdiffraction focal volumes," Phys. Rev. Lett. **94**(17), 178104 (2005).
42. C. Eggeling, K. I. Willig, and F. J. Barrantes, "STED microscopy of living cells--new frontiers in membrane and neurobiology," J. Neurochem. **126**(2), 203–212 (2013).
43. C. Eggeling, C. Ringemann, R. Medda, G. Schwarzmann, K. Sandhoff, S. Polyakova, V. N. Belov, B. Hein, C. von Middendorff, A. Schönle, and S. W. Hell, "Direct observation of the nanoscale dynamics of membrane lipids in a living cell," Nature **457**(7233), 1159–1162 (2009).
44. K. Sozanski, E. Sisamakis, X. Zhang, and R. Holyst, "Quantitative fluorescence correlation spectroscopy in three-dimensional systems under stimulated emission depletion conditions," Optica **4**(8), 982–988 (2017).
45. R. Wollhofen, J. Katzmann, C. Hrelescu, J. Jacak, and T. A. Klar, "120 nm resolution and 55 nm structure size in STED-lithography," Opt. Express **21**(9), 10831–10840 (2013).
46. P. Gao, B. Prunsche, L. Zhou, K. Nienhaus, and G. U. Nienhaus, "Background suppression in fluorescence nanoscopy with stimulated emission double depletion," Nat. Photonics **11**(3), 163–169 (2017).
47. G. Vicidomini, G. Moneron, K. Y. Han, V. Westphal, H. Ta, M. Reuss, J. Engelhardt, C. Eggeling, and S. W. Hell, "Sharper low-power STED nanoscopy by time gating," Nat. Methods **8**(7), 571–573 (2011).
48. L. Lanzanò, I. Coto Hernández, M. Castello, E. Gratton, A. Diaspro, and G. Vicidomini, "Encoding and decoding spatio-temporal information for super-resolution microscopy," Nat. Commun. **6**(1), 6701 (2015).
49. J. Heine, M. Reuss, B. Harke, E. D'Este, S. J. Sahl, and S. W. Hell, "Adaptive-illumination STED nanoscopy," Proc. Natl. Acad. Sci. U.S.A. **114**(37), 9797–9802 (2017).
50. F. Göttfert, T. Pleiner, J. Heine, V. Westphal, D. Görlich, S. J. Sahl, and S. W. Hell, "Strong signal increase in STED fluorescence microscopy by imaging regions of subdiffraction extent," Proc. Natl. Acad. Sci. U.S.A. **114**(9), 2125–2130 (2017).
51. L. Wang, B. Chen, W. Yan, Z. Yang, X. Peng, D. Lin, X. Weng, T. Ye, and J. Qu, "Resolution improvement in STED super-resolution microscopy at low power using a phasor plot approach," Nanoscale **10**(34), 16252–16260 (2018).
52. T. Grotjohann, I. Testa, M. Reuss, T. Brakemann, C. Eggeling, S. W. Hell, and S. Jakobs, "rsEGFP2 enables fast RESOLFT nanoscopy of living cells," eLife **1**, e00248 (2012).
53. F. Balzarotti, Y. Eilers, K. C. Gwosch, A. H. Gynnå, V. Westphal, F. D. Stefani, J. Elf, and S. W. Hell, "Nanometer resolution imaging and tracking of fluorescent molecules with minimal photon fluxes," Science **355**(6325), 606–612 (2017).
54. J. W. Goodman, *Introduction to Fourier optics* (Roberts and Company Publishers, 2005).
55. M. Abramowitz and I. A. Stegun, "Handbook of mathematical function: with formulas, graphs and mathematical tables," in *Handbook of mathematical function: with formulas, graphs and mathematical tables* (Dover Publications, 1965).